catalysts

MDPI

Article

Dual-Function Photocatalysis in the Visible Spectrum: Ag-G-TiO_2 for Simultaneous Dye Wastewater Degradation and Hydrogen Production

Tarek Ahasan, Pei Xu and Huiyao Wang *

Department of Civil Engineering, New Mexico State University, Las Cruces, NM 88003, USA; tarek@nmsu.edu (T.A.); pxu@nmsu.edu (P.X.)
* Correspondence: huiyao@nmsu.edu

Abstract: Photocatalytic processes offer promising solutions for environmental remediation and clean energy production, yet their efficiency under the visible light spectrum remains a significant challenge. Here, we report a novel silver–graphene (Ag-G) modified TiO_2 (Ag-G-TiO_2) nanocomposite photocatalyst that demonstrates remarkably enhanced photocatalytic activity for both dye wastewater degradation and hydrogen production under visible and UV light irradiation. Through comprehensive characterization and performance analysis, we reveal that the Ag-G modification narrows the TiO_2 bandgap from 3.12 eV to 1.79 eV, enabling efficient visible light absorption. The nanocomposite achieves a peak hydrogen production rate of 191 $\mu molesg^{-1}h^{-1}$ in deionized (DI) water dye solution under visible light, significantly outperforming unmodified TiO_2. Intriguingly, we observe an inverse relationship between dye degradation efficiency and hydrogen production rates in dye solutions with tap water versus DI water, highlighting the critical role of water composition in photocatalytic processes. This work not only advances the understanding of fundamental photocatalytic mechanisms but also presents a promising photocatalyst for solar-driven environmental remediation and clean energy production. The Ag-G-TiO_2 nanocomposite's enhanced performance across both visible and UV spectra, coupled with its dual functionality in dye degradation and hydrogen evolution, represents a significant step towards addressing critical challenges in water treatment and sustainable energy generation. Our findings highlight the complex interplay between light absorption and reaction conditions, offering new insights for optimizing photocatalytic systems. This research paves the way for developing more efficient and versatile photocatalysts, potentially contributing to the global transition towards sustainable technologies and circular economy in waste management and energy production.

Keywords: photocatalysis; Ag-G-TiO_2 nanocomposite; dye degradation; hydrogen production; visible and UV light spectrum

Citation: Ahasan, T.; Xu, P.; Wang, H. Dual-Function Photocatalysis in the Visible Spectrum: Ag-G-TiO_2 for Simultaneous Dye Wastewater Degradation and Hydrogen Production. *Catalysts* **2024**, *14*, 530. https://doi.org/10.3390/catal14080530

Academic Editor: Magdalena Janus

Received: 25 July 2024
Revised: 10 August 2024
Accepted: 13 August 2024
Published: 15 August 2024

1. Introduction

The escalating pace of industrialization and urbanization has led to severe water pollution, with various industries—including the food, pharmaceutical, paint, paper, textile, and cosmetic sectors—annually discharging over 10,000 types of synthetic organic dyes into wastewater, totaling more than 10^6 tons globally [1–3]. Effluents laden with persistent dyes and auxiliary chemical additives inflict irreparable harm on aquatic ecosystems and their inhabitants [4]. Methylene blue (MB), a ubiquitous organic dye extensively researched and employed across diverse industrial domains such as textiles, pharmaceuticals, and healthcare, has become a significant wastewater contaminant due to its widespread industrial application, necessitating focused remediation efforts [5,6]. Research has demonstrated that the uncontrolled release of dye-laden effluents into ecosystems poses severe health risks to humans, including carcinogenicity, mutagenicity, and teratogenicity, underscoring the urgent need to develop cost-effective and efficient treatment methodologies for

dye-contaminated wastewater [7]. To mitigate the environmental hazards posed by dye effluents, a spectrum of techniques has been rigorously investigated for the decolorization and decomposition of organic components, encompassing adsorption, membrane filtration, microbial degradation, ozonation, and notably, advanced oxidation processes [8,9]. Despite their widespread application, conventional treatment methods often prove inadequate in reducing dye concentrations to acceptable levels and lack economic viability, highlighting the critical need to develop more effective and cost-efficient dye removal strategies [10].

Photocatalytic processes have emerged as a compelling approach for water purification, addressing the trifecta of cost-effectiveness, environmental sustainability, and energy efficiency requirements for modern treatment technologies [11,12]. This photocatalytic mechanism employs a semiconductor catalyst that, upon light absorption, generates electron–hole pairs. The electrons interact with atmospheric oxygen, producing superoxide radicals, while water molecules enhance the process by allowing hydroxyl ions (OH^-) to react with holes (h^+), forming hydroxyl free radicals (•OH). These highly reactive, non-selective radicals then react with MB, initiating demethylation through the cleavage of N-CH_3 bonds [5].

$$\text{Semiconductor} + h\nu \rightarrow \text{Semiconductor}\ (e^-/h^+) \quad (1)$$

$$O_2 + e^- \rightarrow {}^{\bullet}O_2{}^- \quad (2)$$

$$OH^- + h^+ \rightarrow {}^{\bullet}OH \quad (3)$$

Metal-based heterogeneous catalysts exhibit exceptional efficiency in degrading organic dyes, offering a promising solution for environmental remediation through their ability to effectively break down complex organic structures [13,14].

A synergistic benefit of the photocatalytic process is the concurrent production of hydrogen alongside dye degradation, presenting a dual-purpose approach to wastewater treatment and clean energy generation [15]. The semiconductor, upon light absorption, generates electron–hole pairs that facilitate the dissociation of water molecules into hydrogen and oxygen through photocatalytic water splitting [16,17].

$$\text{Reduction: } 2H^+ + 2e^- \rightarrow H_2 \quad (4)$$

$$\text{Oxidation: } H_2O + 2h^+ \rightarrow 2H^+ + \tfrac{1}{2}\, O_2 \quad (5)$$

Titanium dioxide (TiO_2) stands out as a widely studied photocatalyst, offering numerous advantages and diverse applications. Its exceptional properties, including non-toxicity, high photocatalytic degradation efficiency, and remarkable thermal and chemical stability, make TiO_2 particularly effective for both organic dye degradation in wastewater and hydrogen generation through water splitting [18,19]. Despite its advantages, TiO_2 is constrained by a wide bandgap of 3.2 eV, limiting its photoactivity to the ultraviolet spectrum and rendering it inert under visible light irradiation. Moreover, the rapid recombination of photogenerated electron–hole pairs in pristine TiO_2 significantly impedes its photocatalytic efficiency, presenting a major challenge in its application [5,20].

$$e^- + h^+ \rightarrow \text{heat energy} \rightarrow \text{deactivated semiconductor} \quad (6)$$

To address the limitation posed by the wide bandgap, metal doping is utilized as a dopant for TiO_2 to shift its absorption onset into the visible light region ($\lambda > 400$ nm) [21,22]. This investigation employed silver as a dopant for TiO_2, exploiting its dual capacity to reduce the semiconductor's bandgap and induce surface plasmon resonance. The plasmonic effect on the TiO_2 surface effectively impedes photoexcited electron migration and retards electron–hole pair recombination, consequently augmenting the material's photocatalytic performance [23,24]. Furthermore, graphene oxide was integrated into the TiO_2 matrix, serving a trifold purpose: further reducing the bandgap, enhancing photo-induced charge separation, and facilitating electron mobility within the photocatalytic structure [25].

This study investigates the utilization of synthesized modified and unmodified TiO_2 catalysts for concurrent methylene blue dye wastewater degradation and hydrogen production. We examine the impact of Ag-G modification of TiO_2 on these processes. Methylene blue (MB) dye solutions (10 mg/L) were prepared using deionized (DI) and tap water for experimental use. Two artificial light sources, visible and ultraviolet, were employed as photon energy sources. The incorporation of Ag-G onto TiO_2 demonstrated a marked enhancement in both dye degradation efficiency and hydrogen production rate. Our findings reveal a complex interplay of water chemistry factors that influence the simultaneous dye degradation and hydrogen production processes.

2. Results and Discussion

2.1. Catalyst Characterization

2.1.1. TEM Analysis

Transmission electron microscope (TEM) analysis revealed distinct morphological differences between the pure TiO_2 and Ag-G-TiO_2 samples. While pure TiO_2 particles appeared well dispersed, Ag-G-TiO_2 exhibited an aggregated structure, likely resulting from the deposition of graphene oxide and silver on TiO_2 particles. Particle size distribution analysis corroborated these observations, demonstrating that pure TiO_2 particles had a smaller average size of 21.08 nm, compared to the larger Ag-G-TiO_2 composite particles, which averaged 37.05 nm. This size increase is attributed to the successful incorporation of graphene oxide and silver onto the TiO_2 substrate. Examination of Figure 1B revealed larger, nearly transparent structures consistent with the presence of graphene oxide, as previously reported [23]. From Figure 1C, the distributed dark spots observed in the Ag-G-TiO_2 were identified as silver nanoparticles [26], indicating successful deposition of Ag. EDS analysis provided further confirmation of the presence of silver particles in the composite.

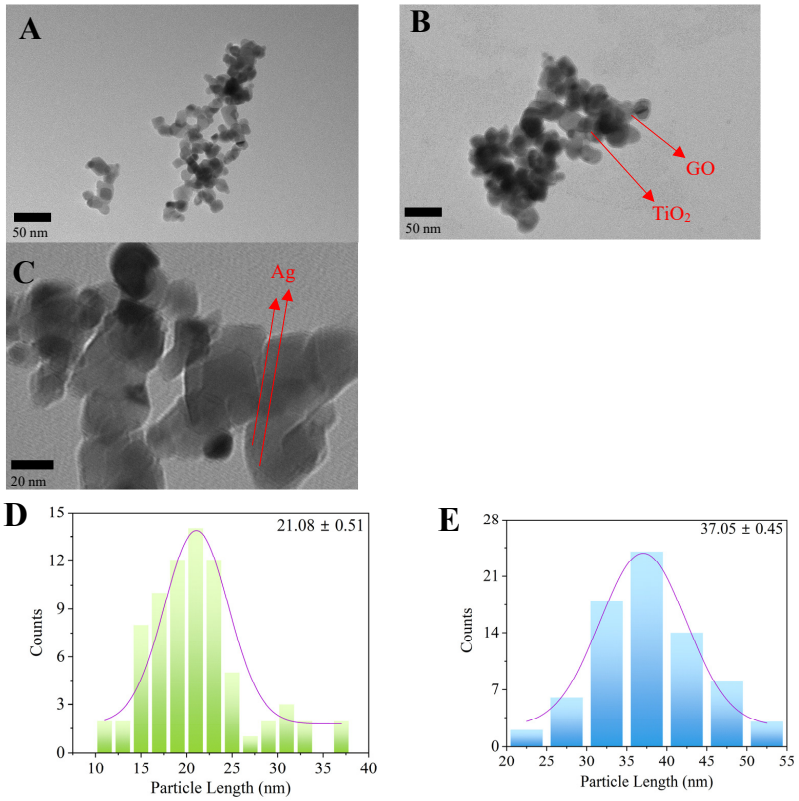

Figure 1. TEM images of the catalysts and their particle size distributions: (**A**) pure TiO_2, (**B**) Ag-G-TiO_2, (**C**) 200K magnification of Ag-G-TiO_2, (**D**) pure TiO_2, (**E**) Ag-G-TiO_2.

2.1.2. EDS Analysis

In Figure 2, the energy dispersive spectroscopy (EDS) analysis provided the quantitative elemental composition of the Ag-G-TiO_2 composite. Titanium constituted the highest weight percentage, at 47.2%, and primarily originated from TiO_2. Oxygen, originating from TiO_2, graphene oxide, $AgNO_3$, and sodium citrate dihydrate, represented 44.1% of the total weight. Carbon, derived from graphene oxide and sodium citrate dihydrate, accounted for 5.9% of the composite mass. Silver comprised 1.9% of the total weight, corroborating the TEM observations of Ag deposition on the TiO_2 particles. A minor sodium content (0.9%) was attributed to the sodium citrate dihydrate used in the synthesis process. These results, in conjunction with the TEM analysis, confirm the successful deposition of Ag on the TiO_2 substrate.

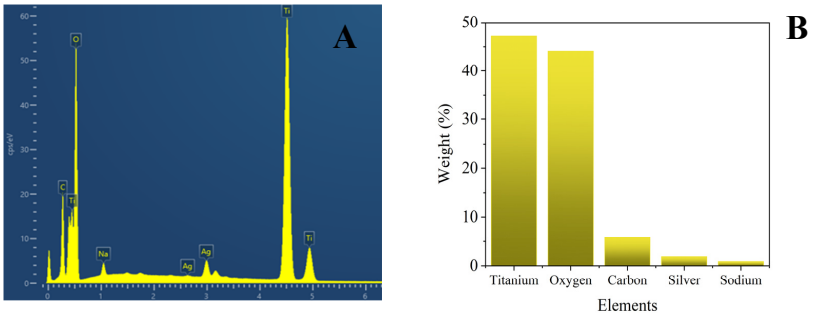

Figure 2. (**A**) EDS analysis of Ag-G-TiO_2, (**B**) weight percentage bar chart of the elements.

2.1.3. XPS Analysis

X-ray photoelectron spectroscopy (XPS) analysis revealed several key insights into the surface chemistry of the materials (Figure 3). The C 1s peak at 283–288 eV was attributed to oxygenated carbon species, likely indicative of graphene oxide incorporation [27]. The peak at ~288 eV suggested the presence of C-O bonds, implying that carbon may have substituted for some lattice titanium atoms, forming a Ti-O-C structure [28]. The carbon content was determined to be 2.43 wt.%. The Ag 3d peak at ~367 eV indicated potential electronic interactions between the metal and the support via charge transfer at the metal–support interface, forming a Ti-Ag-O phase [29]. The silver content was 1.98 wt.% based on the XPS analysis. The weight percentages of Ag determined by the XPS analysis were corroborated by the results of the EDS measurement. The high-resolution Ti 2p spectra (Figure 4A) showed a higher proportion of Ti^{3+} (60.34%) at 458.32 eV compared to Ti^{4+} (30.30%) at 464 eV, suggesting the removal of oxygen from the TiO_2 lattice. Ag doping appeared to increase the Ti^{3+} content while decreasing Ti^{4+}, potentially indicating the formation of Ti_2O_3 or mixed Ag-Ti^{3+} oxide structures [30]. The O 1s spectra displayed two peaks at 529.54 eV and 531.36 eV (Figure 4B), corresponding to Ti-O bonds and oxygen vacancies, respectively. The high density of oxygen vacancies is expected to enhance charge transfer at the interface, improving the overall photocatalytic performance [31]. The peaks at 38 eV and 61 eV are because of the Ti 3p and Ti 3s, respectively [22].

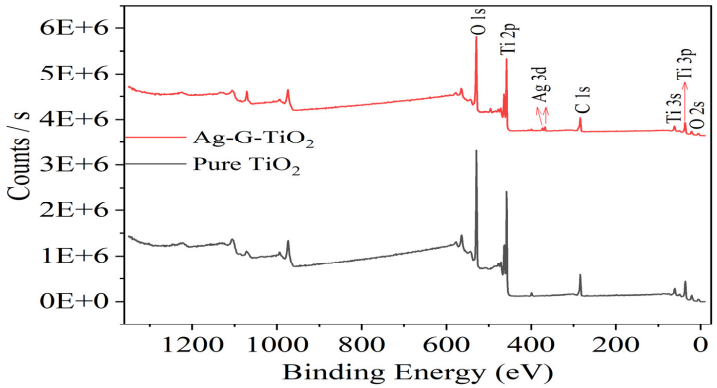

Figure 3. XPS spectra of pure TiO_2 and Ag-G-TiO_2.

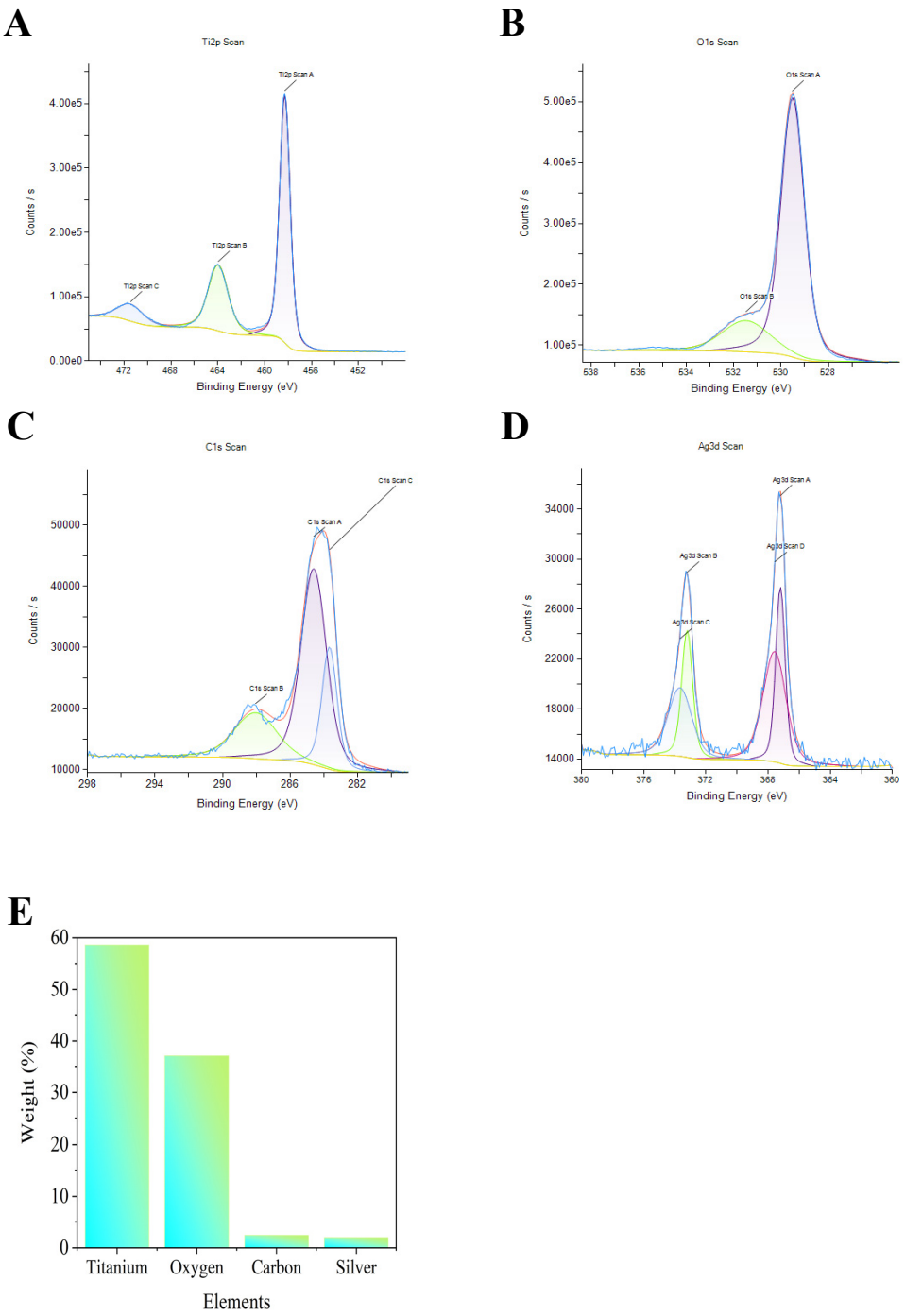

Figure 4. XPS spectra of (**A**) Ti 2p, (**B**) O 1s, (**C**) C 1s, (**D**) Ag 3d, (**E**) Elemental weight percentage.

2.1.4. Bandgap Analysis

UV–vis spectroscopy revealed that the absorption edge for TiO_2 occurred at 385 nm, while for Ag-G-TiO_2, it redshifted to 494 nm. This redshift indicates the presence of electron acceptors, likely due to the surface plasmon absorption of Ag^0. The observed absorption phenomenon can be attributed to charge transfer from the valence band to the conduction band, specifically, the transition of electrons from 2p orbitals of oxide anions to 3d orbitals of Ti^{4+} cations [32]. Bandgap calculations showed a significant reduction from 3.12 eV for pure TiO_2 (Figure 5A) to 1.79 eV for Ag-G-TiO_2 (Figure 5B). This narrowing of the bandgap in the nanocomposite facilitates the effective assimilation of photoinduced electrons, resulting in the formation of a closed Fermi level energy between the valence and conduction bands [33]. The consequent decrease in Fermi energy promotes

the migration and separation of photoinduced electron–hole pairs, potentially enhancing the photocatalytic performance of the catalyst [33].

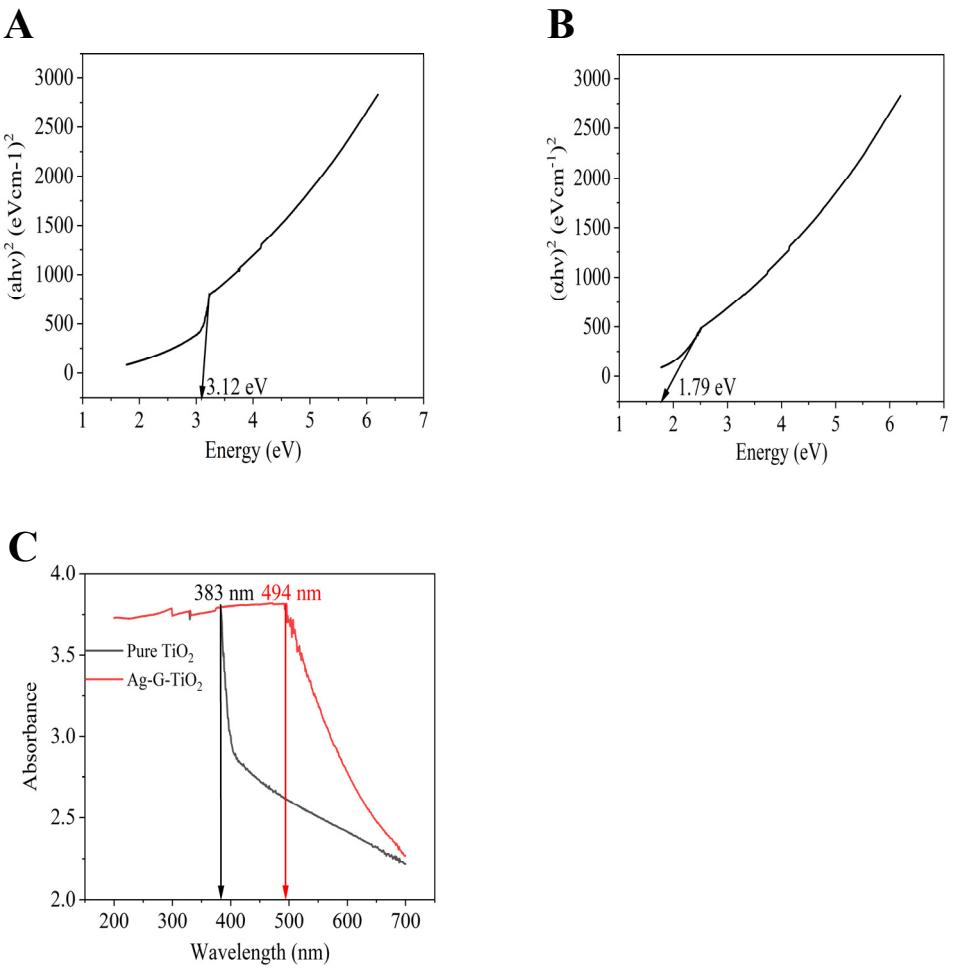

Figure 5. Bandgap analysis of the catalysts: (**A**) pure TiO_2, (**B**) Ag-G-TiO_2, (**C**) Absorbance comparison between pure TiO_2 and Ag-G-TiO_2.

2.1.5. XRD Analysis

X-ray diffraction (XRD) analysis was employed to determine the crystal phase and crystallite size of both unmodified TiO_2 and Ag-G-TiO_2 (Figure 6). Both samples exhibited characteristic peaks corresponding to anatase (JCPDS 78-2486) and rutile (JCPDS 21-1276) phases [34]. Notably, diffraction peaks attributable to Ag were not observed in the Ag-G-TiO_2 sample, likely due to its low concentration [35]. Typically, XRD peaks associated with Ag appear at 38.1° and 64.5° when the Ag doping exceeds 2 wt% [36]. A slight shift in the primary TiO_2 peak from 25.10° to 24.93° was observed, suggesting the incorporation of Ag^+ ions into the Ti^{4+} lattice [37]. The rutile phase content was calculated using the following equation:

$$\text{Rutile phase content (\%)} = A_R/(0.884 \times (A_A + A_R)) \quad (7)$$

where A_A and A_R represent the integrated intensities of the diffraction peaks from the (101) and (110) planes of the anatase and rutile phases, respectively. Upon Ag doping, a slight decrease in the anatase phase of TiO_2 was observed, as shown in Table 1. This finding aligns with previous reports in the literature [38].

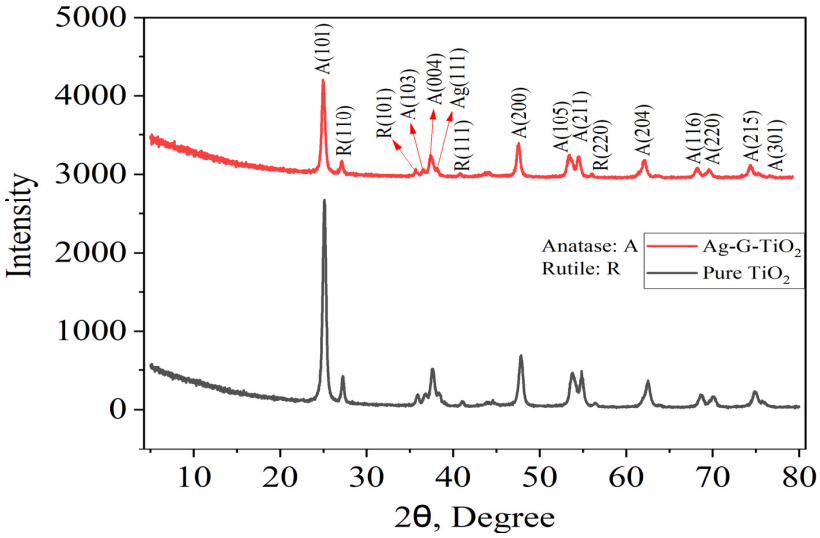

Figure 6. XRD patterns of the pure TiO_2 and Ag-G-TiO_2.

Table 1. Crystalline phase compositions of the photocatalysts.

Photocatalysts	Crystalline Phase, %	
	Anatase	Rutile
TiO_2	89.23	10.77
Ag-G-TiO_2	88.89	11.11

2.1.6. Nitrogen Adsorption–Desorption Analysis

The nitrogen adsorption–desorption isotherm for the synthesized catalyst exhibited a Type IV profile (Figure 7). Initially, the nitrogen uptake was low, but it increased rapidly when the relative pressure exceeded 0.8. This isotherm shape is characteristic of mesoporous materials. The Brunauer–Emmett–Teller (BET) surface area of the synthesized catalyst was determined to be 69.01 m^2/g, which is significantly higher than the 37.56 m^2/g surface area of pure TiO_2 [39]. This enhancement is likely due to the incorporation of graphene oxide into the catalyst structure [40]. Analysis of the pore size distribution revealed an average Barrett–Joyner–Halenda (BJH) adsorption pore diameter of 55.02 Å and an average BJH desorption pore diameter of 225.58 Å, indicating that the catalyst contained predominantly mesoporous features (Table 2). The Langmuir surface area of the catalyst was determined to be 45.67 m^2/g.

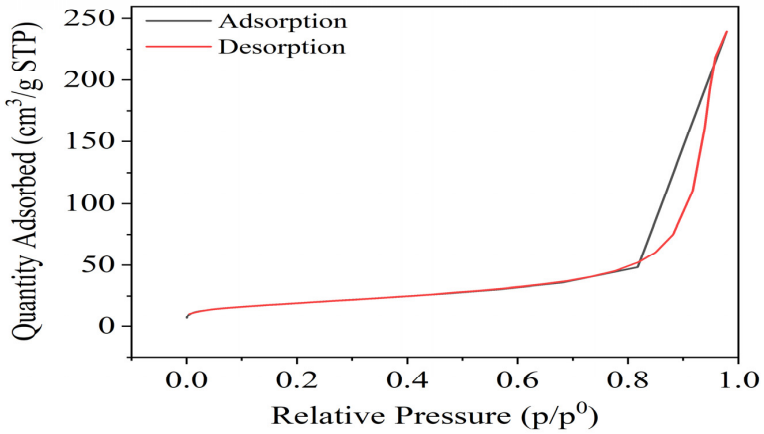

Figure 7. Adsorption isotherm of Ag-G-TiO_2 catalyst.

Table 2. Surface area and porosity of the synthesized catalyst.

BET Surface Area	69.01 m^2/g
Langmuir surface area	45.67 m^2/g
BJH adsorption cumulative pore volume	0.065 cm^3/g
BJH desorption cumulative pore volume	0.388 cm^3/g
BJH adsorption average pore diameter	55.02 Å
BJH desorption average pore diameter	225.58 Å

2.2. Photocatalytic Dye Wastewater Degradation

The visible light experiments revealed rapid dye degradation within the first hour using the Ag-G-TiO_2 catalyst, indicating efficient purification (Figure 8). In contrast, TiO_2 alone exhibited a significantly slower degradation rate under visible light. This performance disparity suggests that silver and graphene modifications enhance purification efficiency by lowering the catalyst's bandgap, enabling visible light absorption. The photocatalytic excitation of the catalyst generated electron–hole pairs, and the photoexcited electrons interacted with oxygen to form reactive superoxide radicals ($^{\bullet}O_2^-$), while the photogenerated holes reacted with water molecules or hydroxyl ions to produce hydroxyl radicals ($^{\bullet}OH$). These highly reactive species subsequently interacted with methylene blue molecules, leading to the degradation of the dye [41,42]. Optimal dye degradation was achieved using Ag-G-TiO_2 in tap water, with dye concentration decreasing from 10 mg/L to 0.03 mg/L over 6 h, yielding 97% efficiency. Under identical conditions with DI water, the concentration decreased to 1.67 mg/L, corresponding to 83.3% efficiency. Similar trends were observed with pure TiO_2, indicating higher performance in tap water thanin DI water. This difference may be attributed to the presence of ions or compounds in tap water acting as sacrificial agents, facilitating electron migration and the separation of charge carriers [43]. Extended experiments beyond 12 h showed convergence to low concentration ratios across all conditions, suggesting high overall purification efficiency regardless of the specific treatment.

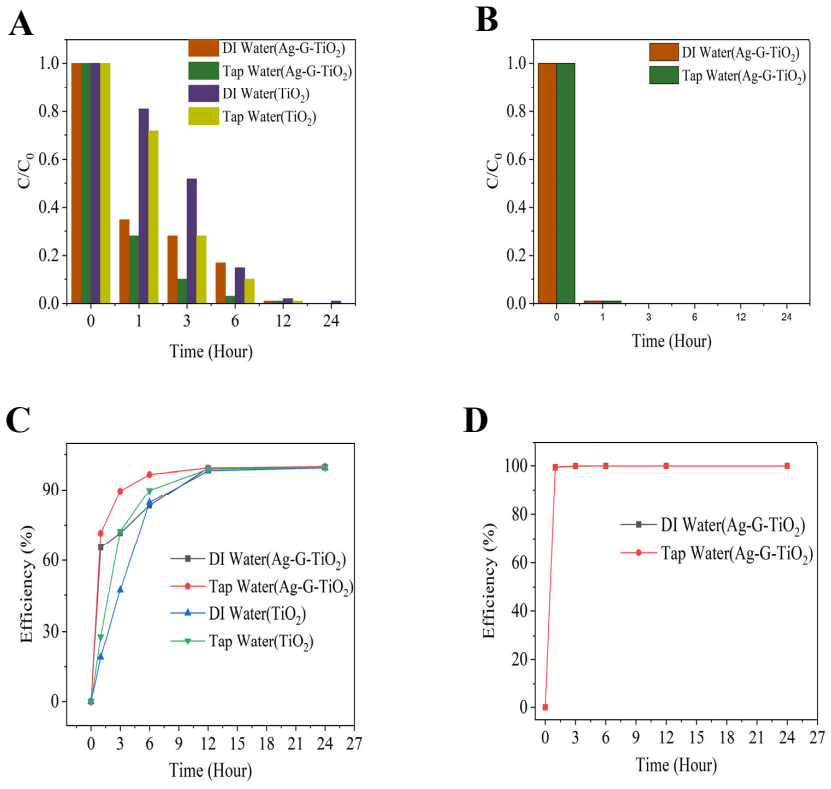

Figure 8. Photocatalytic dye wastewater degradation and catalyst efficiency over time. (**A**) Visible light, (**B**) UV light, (**C**) visible light, (**D**) UV light.

TiO_2 becomes an active semiconductor under UV irradiation (<400 nm) [44]. UV light experiments demonstrated an extremely rapid decrease in concentration ratio (C/C_0) for both DI and tap water solutions within the first hour. This indicates a faster and more effective purification process compared to that of visible light. Under UV irradiation, dye concentration decreased from 10 mg/L to 0.06 mg/L (DI) and 0.05 mg/L (tap), corresponding to efficiencies of 99.43% and 99.50%, respectively. The marked difference between visible and UV light performance can be attributed to the superior activation of Ag-G-TiO_2 under UV light, which more effectively generates electron–hole pairs on the catalyst surface, leading to rapid formation of reactive oxygen species for dye degradation. The enhanced performance under visible light indicates that the Ag-G modification of TiO_2 successfully extended the photocatalyst's activity into the visible spectrum. This improvement is likely due to a reduced bandgap, which facilitates more efficient electron–hole pair generation and separation [45].

2.3. Photocatalytic Hydrogen Production

Photocatalytic hydrogen production experiments revealed significant differences between modified (Ag-G-TiO_2) and unmodified TiO_2 catalysts under both visible and UV light conditions (Figure 9). The Ag-G-TiO_2 catalyst demonstrated markedly superior activity, indicating the profound impact of graphene and silver modification on catalytic performance. Under visible light irradiation, Ag-G-TiO_2 achieved a peak hydrogen production rate of 191 μmoles g^{-1} h^{-1} in DI water dye solution, which was substantially higher than the 108 μmoles g^{-1} h^{-1} observed in tap water (Figure 9A). This trend was consistent across both catalyst types and light sources, with DI water consistently outperforming tap water in terms of hydrogen evolution. Intriguingly, while dye degradation efficiency was superior in tap water (Figure 8C), hydrogen production rates were lower compared to DI water. This inverse relationship may be attributed to the presence of ions and compounds in tap water that potentially adsorb onto the catalyst surface, blocking active sites for hydrogen evolution [46]. Furthermore, these species might engage in competitive reactions, consuming some of the photogenerated electrons and reducing their availability for hydrogen production [47].

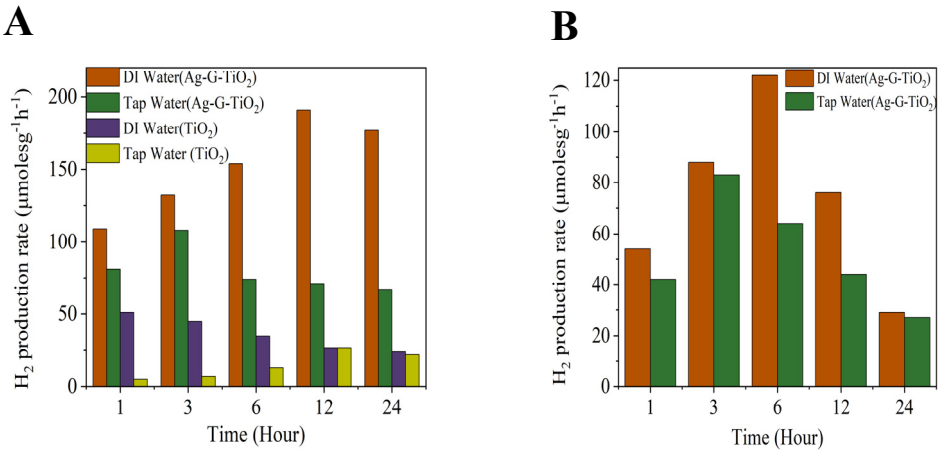

Figure 9. Photocatalytic hydrogen production. (**A**) Visible light, (**B**) UV light.

Comparative analysis of the visible and UV light experiments revealed distinct kinetic profiles. UV irradiation induced a more rapid initial hydrogen production rate, whereas visible light facilitated more sustained production, ultimately achieving the highest overall rate. Both conditions exhibited a decline in production rate after peak performance (6 h for UV, 12 h for visible light), potentially indicating photocorrosion of the catalyst [48,49]. The accelerated dye degradation under UV light may have contributed to catalyst degradation, resulting in a lower hydrogen production rate compared to visible light conditions.

3. Materials and Methods

3.1. Preparation of 2 Millimole Silver Nitrate (2 mM $AgNO_3$)

A 2 mM $AgNO_3$ solution was prepared by dissolving 0.17 g of $AgNO_3$ (ACS reagent, ≥99.0%, Sigma Aldrich, Darmstadt, Germany) in 500 mL of DI water. To ensure complete dissolution, the mixture was subjected to continuous stirring at 500 rpm for a duration of 30 min.

3.2. Preparation of 2 Millimole Sodium Citrate Dihydrate

To prepare a 2 mM sodium citrate solution, 0.294 g of sodium citrate dihydrate (granular certified, Fisher Chemical, Pittsburgh, PA, USA) was dissolved in 500 mL of DI water. The mixture underwent continuous agitation for 30 min to ensure complete solubilization.

3.3. Synthesis of Silver–Graphene-TiO_2 (Ag-G-TiO_2) Catalyst

The synthesis of the nanocomposite catalyst began with the dispersion of TiO_2 (P25, primary particle size 21 nm, ≥99.5%, Sigma Aldrich, Darmstadt, Germany) in a mixture of 60 mL DI water and 30 mL ethanol (ACS reagent, ≥99.5%, Sigma Aldrich). Ethanol inclusion enhanced TiO_2 particle dispersion in the aqueous medium [50]. Subsequently, 5 mL of graphene oxide aqueous dispersion (5 mg/mL) was introduced into the suspension. The resulting mixture underwent sonication for 1 h to ensure homogeneous component distribution. Following sonication, the mixture was subjected to a hydrothermal reaction at 120 °C for 24 h, during which the solution color transitioned from off-white to dark blue. The product was then purified via centrifugation, performed five times at 1500 rpm for 10 min each, using DI water. The purified product was then combined with 30 mL of 2 mM $AgNO_3$ solution and 30 mL of 2 mM sodium citrate dihydrate solution. This mixture underwent microwave (Hamilton Beach, 700 W, Shenzhen, China) irradiation for 3 min at 50% power (350 W). Microwave treatment facilitates rapid, volumetric, and uniform heating, resulting in improved structural and morphological characteristics of the synthesized nanomaterials [51,52]. Finally, the product was dried in an oven at 60 °C for 24 h to obtain the final catalyst.

3.4. Characterization of the Catalyst

3.4.1. TEM Analysis

Structural and morphological characterization of the TiO_2 and Ag-G-TiO_2 samples was conducted using an H-7650 Transmission Electron Microscope (TEM) (Hitachi High-Tech America, Inc., Pleasanton, CA, USA). Sample preparation involved depositing dry catalyst powder onto a holey carbon film supported by a 200-mesh copper TEM grid. TEM analysis facilitated the measurement of nanoparticle dimensions. Quantitative analysis of particle size distribution was performed using ImageJ software 1.50d, which enabled the determination of nanoparticle diameters, generation of size histograms, and calculation of standard deviations. The mean particle dimensions of the pristine TiO_2 and Ag-G-TiO_2 samples were determined through analysis using Origin software 2023.

3.4.2. XRD Analysis

Crystalline phase analysis of the catalyst was performed using an Empyrean Powder Diffractometer (PANalytical, The Netherlands). XRD spectra were acquired by scanning 0.5 g of the catalyst, placed in a sample holder, over a 2θ range of 5° to 80° at a rate of 0.11 deg/s in reflection mode. The diffraction patterns were plotted as intensity versus diffraction angle (2θ). Highscore software 3.0.5 was employed for spectral analysis, and the resultant XRD profiles were compared with literature data for phase identification.

3.4.3. Bandgap Analysis

Bandgap determination for the catalysts (TiO_2 and Ag-G-TiO_2) was conducted using a HACH DR6000 ultraviolet–visible spectrophotometer (Loveland, CO, USA). Samples were prepared by dispersing 0.05 g of catalyst in 50 mL of DI water. Absorbance spectra were

acquired over a wavelength range of 200–700 nm. Bandgap analysis employed the Tauc plot method [53], utilizing the following equation:

$$(\alpha h\nu)^{1/\gamma} = B(h\nu - Eg)$$

where α represents the energy-dependent absorption coefficient, h is Planck's constant, ν denotes the incident photon frequency, Eg is the bandgap energy, and B is a constant. The γ factor indicates the nature of the electronic transition: $\gamma = 2$ for direct transitions and $\gamma = 1/2$ for indirect transitions. The transition type was determined by comparing the goodness of fit for plots of $(\alpha h\nu)^{1/\gamma}$ versus $(h\nu)$ using both γ values.

3.4.4. EDS Analysis

Elemental composition analysis was performed using Energy-Dispersive X-ray Spectroscopy (EDS) with an Ultra-High-Resolution Schottky Scanning Electron Microscope SU7000 (Hitachi High-Tech America, Inc., Pleasanton, CA, USA), equipped with an Ultim Max EDS detector. Sample preparation involved adhering approximately 0.2 g of the catalyst to double-sided carbon tape affixed to the sample holder. The EDS analysis was conducted at an accelerating voltage of 15 kV.

3.4.5. XPS Analysis

XPS analysis was performed on the TiO_2 and Ag-G-TiO_2 nanoparticles using a Kratos Axis 165 Ultra Photoelectron Spectrometer/Surface Analysis system (Kratos Analytical, Manchester, UK). This instrument is equipped with a monochromatized Al Kα X-ray source and was operated at 15 keV and a 20 mA emission current. All survey spectra were collected in constant analyzer energy mode with a pass energy of 160 eV. Individual spectral regions were acquired at pass energy of 20 eV using the hybrid lens mode, which combines electrostatic and magnetic immersion electron collection optics. The catalysts were prepared for analysis by uniformly dispersing them on a piece of carbon tape, which was then mounted on the sample holder.

3.4.6. Nitrogen Adsorption–Desorption Analysis

The porosity and specific surface area of the materials were determined from nitrogen adsorption–desorption isotherms measured at −196.928 °C. Prior to analysis, the samples were degassed at 60 °C using a Micromeritics Smart Vacprep system (Norcross, GA, USA). The nitrogen adsorption–desorption isotherms were then obtained using a Micromeritics ASAP 2050 adsorption analyzer (Norcross, GA, USA), and the equilibration interval was 20 s.

3.5. Preparation of Dye Solution

Methylene blue dye (Baker analyzed reagent, J.T. Baker Chemical Co., Phillipsburg, NJ, USA) was used to prepare two 10 mg/L solutions, one in DI water and another in tap water. The conductivity of the dye solution using DI water was 2.8 µS/cm and the conductivity of the dye solution using tap water was 685 µS/cm. A series of standard solutions with concentrations of 2.5, 5, 10, and 20 mg/L were also prepared. Absorbance measurements were obtained using a HACH DR6000 ultraviolet–visible spectrophotometer (Loveland, CO, USA). A calibration curve was constructed in Excel to determine the final dye concentrations following the experimental procedure.

3.6. Experimental Setup and Photocatalytic Activity Test

The photocatalytic experiments were conducted in a 50 mL quartz round-bottom flask reactor. For each experiment, 50 mL of the dye solution was introduced into the reactor, followed by the addition of 0.01 g of catalyst. To ensure homogeneous dispersion of the catalyst, the system was subjected to ultrasonication for 10 min in a dark condition achieved by covering the sonication instrument. Two light sources were employed: a high-pressure UV mercury vapor lamp (160 W PUV-10, Zoo Med Laboratories, San Luis Obispo, CA,

USA) for UV irradiation, and an R40 Dimmable Mercury-Free Incandescent Heat Lamp (250 W, KOR Lighting, Miami, FL, USA) for visible light experiments. The tightly sealed reactors were positioned 6 inches away from the light source on a magnetic stirrer, maintaining continuous agitation at 400 rpm throughout the experiment. Separate experiments were conducted for durations of 1, 3, 6, 12, and 24 h to assess the progression of the photocatalytic reaction over time. The efficiency of dye degradation was quantified using the following equation:

$$E = (1 - C/C_0) \times 100$$

where E represents the degradation efficiency (%), C denotes the dye concentration after a specific experimental duration, and C_0 is the initial dye concentration.

3.7. Hydrogen Gas Analysis

Hydrogen gas production was analyzed using an Agilent 7890A gas chromatograph (GC, Santa Clara, CA, USA) equipped with a thermal conductivity detector (TCD) and an HP-5 molecular sieve column. Nitrogen was employed as the carrier gas. The instrument was calibrated using a pure H_2 standard. For each analysis, 1 mL of headspace gas was injected directly into the GC inlet. The method parameters included a purge time of 1 min, followed by a 10 min chromatographic run post-injection. Quantification of hydrogen was achieved by comparing the retention time and peak area of the sample to that of the H_2 standard. After the completion of the specific time experiments, UV absorbance and hydrogen production readings over time were taken immediately.

4. Conclusions

This study demonstrates the significant enhancement of photocatalytic performance achieved through the modification of TiO_2 with silver and graphene (Ag-G-TiO_2). Our findings reveal a complex interplay between catalyst composition, irradiation wavelength, and water chemistry in both dye wastewater degradation and hydrogen production processes. The Ag-G-TiO_2 nanocomposite exhibited superior photocatalytic activity compared to pure TiO_2, particularly under visible light. This enhancement is attributed to the narrowing of the bandgap from 3.12 eV to 1.79 eV, facilitating more efficient light absorption and charge carrier separation. The synergistic effects of plasmonic silver nanoparticles and graphene sheets contribute to extended light absorption and improved electron transport, respectively. Intriguingly, we observed an inverse relationship between dye degradation efficiency and hydrogen production rates in tap water versus DI water. This phenomenon highlights the critical role of water composition in determining the dominant photocatalytic pathway and suggests potential strategies for optimizing either water treatment or hydrogen production applications.

The sustained hydrogen production under visible light coupled with the rapid initial rates under UV irradiation underscore the versatility of the Ag-G-TiO_2 catalyst. However, the observed decline in production rate over time highlights the need for further research into catalyst stability and regeneration strategies. Future work should focus on elucidating the precise mechanisms of charge transfer and reactive species generation; optimizing catalyst composition for specific applications; and exploring strategies to mitigate photocorrosion effects. Additionally, scaling up these systems for practical implementation remains an important challenge that needs to be addressed.

5. Patents

A patent for this research has been applied for.

Author Contributions: Conceptualization, H.W. and P.X.; methodology, H.W. and T.A.; software, T.A.; validation, H.W. and T.A.; formal analysis, T.A.; investigation, T.A. and H.W.; data curation, T.A.; writing—original draft preparation, T.A.; writing—review and editing, H.W. and P.X.; visualization, T.A.; supervision, H.W.; project administration, H.W.; funding acquisition, H.W. All authors have read and agreed to the published version of the manuscript.

Funding: This research was partially funded by the New Mexico Water Resources Research Institute, grant number NMWRRI-SG-FALL2023.

Data Availability Statement: All data are presented in the main text.

Acknowledgments: We would like to acknowledge the financial support from NSF for the acquisition of the XPS equipment (NSF/CHEM 2216473), and the support from the XPS Surface Characterization Facility at UTEP.

Conflicts of Interest: The authors declare no conflicts of interest.

References

1. Behera, A.K.; Shadangi, K.P.; Sarangi, P.K. Efficient removal of Rhodamine B dye using biochar as an adsorbent: Study the performance, kinetics, thermodynamics, adsorption isotherms and its reusability. *Chemosphere* **2024**, *354*, 141702. [CrossRef] [PubMed]
2. Oladoye, P.O.; Ajiboye, T.O.; Omotola, E.O.; Oyewola, O.J. Methylene blue dye: Toxicity and potential elimination technology from wastewater. *Results Eng.* **2022**, *16*, 100678. [CrossRef]
3. Alver, E.; Metin, A.Ü.; Brouers, F. Methylene blue adsorption on magnetic alginate/rice husk bio-composite. *Int. J. Biol. Macromol.* **2020**, *154*, 104–113. [CrossRef] [PubMed]
4. Yang, J.; Han, Y.; Sun, Z.; Zhao, X.; Chen, F.; Wu, T.; Jiang, Y. PEG/sodium tripolyphosphate-modified chitosan/activated carbon membrane for rhodamine B removal. *ACS Omega* **2021**, *6*, 15885–15891. [CrossRef] [PubMed]
5. Din, M.I.; Khalid, R.; Najeeb, J.; Hussain, Z. Fundamentals and photocatalysis of methylene blue dye using various nanocatalytic assemblies—A critical review. *J. Clean. Prod.* **2021**, *298*, 126567. [CrossRef]
6. Muzammal, S.; Ahmad, A.; Sheraz, M.; Kim, J.; Ali, S.; Hanif, M.B.; Hussain, I.; Pandiaraj, S.; Alodhayb, A.; Javed, M.S.; et al. Polymer-supported nanomaterials for photodegradation: Unraveling the methylene blue menace. *Energy Convers. Manag. X* **2024**, *22*, 100547. [CrossRef]
7. Yao, X.; Fang, Y.; Guo, Y.; Xu, M. Degradation of methylene blue using a novel gas-liquid hybrid DDBD reactor: Performance and pathways. *Chemosphere* **2023**, *336*, 139172. [CrossRef]
8. Deng, F.; Brillas, E. Advances in the decontamination of wastewaters with synthetic organic dyes by electrochemical Fenton-based processes. *Sep. Purif. Technol.* **2023**, *316*, 123764. [CrossRef]
9. Alardhi, S.M.; Salih, H.G.; Ali, N.S.; Khalbas, A.H.; Salih, I.K.; Saady, N.M.C.; Zendehboudi, S.; Albayati, T.M.; Harharah, H.N. Olive stone as an eco-friendly bio-adsorbent for elimination of methylene blue dye from industrial wastewater. *Sci. Rep.* **2023**, *13*, 21063. [CrossRef] [PubMed]
10. Jabbar, N.M.; Alardhi, S.M.; Mohammed, A.K.; Salih, I.K.; Albayati, T.M. Challenges in the implementation of bioremediation processes in petroleum-contaminated soils: A review. *Environ. Nanotechnol. Monit. Manag.* **2022**, *18*, 100694. [CrossRef]
11. Swain, J.; Priyadarshini, A.; Hajra, S.; Panda, S.; Panda, J.; Samantaray, R.; Yamauchi, Y.; Han, M.; Kim, H.J.; Sahu, R. Photocatalytic dye degradation by $BaTiO_3$/zeolitic imidazolate framework composite. *Alloys Compd.* **2023**, *965*, 171438. [CrossRef]
12. Lee, D.E.; Kim, M.K.; Danish, M.; Jo, W.K. State-of-the-art review on photocatalysis for efficient wastewater treatment: Attractive approach in photocatalyst design and parameters affecting the photocatalytic degradation. *Catal. Commun.* **2023**, *183*, 106764. [CrossRef]
13. Wang, D.; Li, Y.; Wen, L.; Xi, J.; Liu, P.; Hansen, T.W.; Li, P. Ni-Pd-incorporated Fe_3O_4 yolk-shelled nanospheres as efficient magnetically recyclable catalysts for reduction of n-containing unsaturated compounds. *Catalysts* **2023**, *13*, 190. [CrossRef]
14. Guo, S.; Chen, M.; Wei, Y.; You, L.; Cai, C.; Wei, Q.; Zhou, K. Designing hierarchically porous zero-valent iron via 3D printing to degrade organic pollutants by activating peroxymonosulfate using high-valent iron-oxo species. *Chem. Eng. J.* **2023**, *476*, 146523. [CrossRef]
15. Gonuguntla, S.; Kamesh, R.; Pal, U.; Chatterjee, D. Dye sensitization of TiO_2 relevant to photocatalytic hydrogen generation: Current research trends and prospects. *JPPC* **2023**, *57*, 100621. [CrossRef]
16. Nyamai, N.; Phaahlamohlaka, T. Significantly advanced hydrogen production via water splitting over Zn/TiO_2/CNFs and Cu/TiO_2/CNFs nanocomposites. *J. Ind. Eng. Chem.* **2024**, *134*, 312–326. [CrossRef]
17. Deng, A.; Sun, Y.; Gao, Z.; Yang, S.; Liu, Y.; He, H.; Zhang, J.; Liu, S.; Sun, H.; Wang, S. Internal electric field in carbon nitride-based heterojunctions for photocatalysis. *Nano Energy* **2023**, *108*, 108228. [CrossRef]
18. Sari, Y.; Gareso, P.L.; Armynah, B.; Tahir, D. A review of TiO_2 photocatalyst for organic degradation and sustainable hydrogen energy production. *Int. J. Hydrogen Energy* **2023**, *55*, 984–996. [CrossRef]
19. Chen, Y.; Soler, L.; Cazorla, C.; Oliveras, J.; Bastús, N.G.; Puntes, V.F.; Llorca, J. Facet-engineered TiO_2 drives photocatalytic activity and stability of supported noble metal clusters during H_2 evolution. *Nat. Commun.* **2023**, *14*, 6165. [CrossRef]
20. Rashid, R.; Shafiq, I.; Gilani, M.R.H.S.; Maaz, M.; Akhter, P.; Hussain, M.; Jeong, K.-E.; Kwon, E.E.; Bae, S.; Park, Y.-K. Advancements in TiO_2-based photocatalysis for environmental remediation: Strategies for enhancing visible-light-driven activity. *Chemosphere* **2023**, *349*, 140703. [CrossRef]
21. Ahmed, T.Y.; Aziz, S.B.; Dannoun, E.M.A. Role of Outer shell Electron-Nuclear Distant of Transition Metal Atoms (TMA) on Band Gap Reduction and Optical Properties of TiO_2 Semiconductor. *Results Eng.* **2024**, *23*, 102479. [CrossRef]

22. Edirisooriya, E.M.N.T.; Senanayake, P.S.; Wang, H.B.; Talipov, M.R.; Xu, P.; Wang, H. Photo-reforming and degradation of waste plastics under UV and visible light for H_2 production using nanocomposite photocatalysts. *J. Environ. Chem. Eng.* **2023**, *11*, 109580. [CrossRef]
23. Liza, T.Z.; Tusher, M.M.H.; Anwar, F.; Monika, M.F.; Amin, K.F.; Asrafuzzaman, F.N.U. Effect of Ag-doping on morphology, structure, band gap and photocatalytic activity of bio-mediated TiO_2 nanoparticles. *Results Mater.* **2024**, *22*, 100559. [CrossRef]
24. Sukhadeve, G.K.; Bandewar, H.; Janbandhu, S.Y.; Jayaramaiah, J.R.; Gedam, R.S. Photocatalytic hydrogen production, dye degradation, and antimicrobial activity by Ag-Fe co-doped TiO_2 nanoparticles. *J. Mol. Liq.* **2023**, *369*, 120948. [CrossRef]
25. Lin, L.; Wang, H.; Xu, P. Immobilized TiO_2-reduced graphene oxide nanocomposites on optical fibers as high performance photocatalysts for degradation of pharmaceuticals. *Chem. Eng. J.* **2017**, *310*, 389–398. [CrossRef]
26. Gogoi, D.; Namdeo, A.; Golder, A.K.; Peela, N.R. Ag-doped TiO_2 photocatalysts with effective charge transfer for highly efficient hydrogen production through water splitting. *Int. J. Hydrogen Energy* **2020**, *45*, 2729–2744. [CrossRef]
27. Akhavan, O.; Abdolahad, M.; Esfandiar, A.; Mohatashamifar, M. Photodegradation of graphene oxide sheets by TiO_2 nanoparticles after a photocatalytic reduction. *J. Phys. Chem. C* **2010**, *114*, 12955–12959. [CrossRef]
28. Ren, W.; Ai, Z.; Jia, F.; Zhang, L.; Fan, X.; Zou, Z. Low temperature preparation and visible light photocatalytic activity of mesoporous carbon-doped crystalline TiO_2. *Appl. Catal. B Environ.* **2007**, *69*, 138–144. [CrossRef]
29. *NIST X-ray Photoelectron Spectrosc Database*, Version 35; NIST: Gaithersburg, MD, USA, 2014.
30. Bharti, B.; Kumar, S.; Lee, H.-N.; Kumar, R. Formation of oxygen vacancies and Ti^{3+} state in TiO_2 thin film and enhanced optical properties by air plasma treatment. *Sci. Rep.* **2016**, *6*, 32355. [CrossRef]
31. Paul, K.K.; Giri, P.K. Role of surface plasmons and hot electrons on the multi-step photocatalytic decay by defect enriched Ag@ TiO_2 nanorods under visible light. *J. Phys. Chem. C* **2017**, *121*, 20016–20030. [CrossRef]
32. Rathi, V.H.; Jeice, A.R.; Jayakumar, K. Green synthesis of Ag/CuO and Ag/TiO_2 nanoparticles for enhanced photocatalytic dye degradation, antibacterial, and antifungal properties. *Appl. Surf. Sci. Adv.* **2023**, *18*, 100476. [CrossRef]
33. Jadhav, S.; Kalubarme, R.; Chauhan, R.; Singh, A.; Kale, B.; Ashokkumar, M.; Gosavi, S. Nanocrystalline Ag-doped cobalt oxide as a flexible electrode material for high performance supercapacitor application. *J. Energy Storage* **2023**, *58*, 106326. [CrossRef]
34. Liu, W.; Chen, D.; Yoo, S.H.; Cho, S.O. Hierarchical visible-light-response Ag/AgCl@ TiO_2 plasmonic photocatalysts for organic dye degradation. *Nanotechnology* **2013**, *24*, 405706. [CrossRef]
35. Santos, L.M.; Machado, W.A.; França, M.D.; Borges, K.A.; Paniago, R.M.; Patrocinio, A.O.T.; Machado, A.E.H. Structural characterization of Ag-doped TiO_2 with enhanced photocatalytic activity. *RSC Adv.* **2015**, *5*, 103752–103759. [CrossRef]
36. Ali, T.; Ahmed, A.; Alam, U.; Uddin, I.; Tripathi, P.; Muneer, M. Enhanced photocatalytic and antibacterial activities of Ag-doped TiO_2 nanoparticles under visible light. *Mater. Chem. Phys.* **2018**, *212*, 325–335. [CrossRef]
37. Rabhi, S.; Belkacemi, H.; Bououdina, M.; Kerrami, A.; Brahem, L.A.; Sakher, E. Effect of Ag doping of TiO_2 nanoparticles on anatase-rutile phase transformation and excellent photodegradation of amlodipine besylate. *Mater. Lett.* **2019**, *236*, 640–643. [CrossRef]
38. Mogal, S.I.; Gandhi, V.G.; Mishra, M.; Tripathi, S.; Shripathi, T.; Joshi, P.A.; Shah, D.O. Single-step synthesis of silver-doped titanium dioxide: Influence of silver on structural, textural, and photocatalytic properties. *Ind. Eng. Chem. Res.* **2014**, *53*, 5749–5758. [CrossRef]
39. Abla, F.; Elsayed, Y.; Farha, N.A.; Obaideen, K.; Mohamed, A.A.; Lee, H.; Han, C.; Egilmez, M.; Kanan, S. Fabrication of high surface area TiO_2-MoO_3 nanocomposite as a photocatalyst for organic pollutants removal from water bodies. *Catalysts* **2023**, *13*, 362. [CrossRef]
40. Altass, H.M.; Morad, M.; Khder, A.E.R.S.; Mannaa, M.A.; Jassas, R.S.; Alsimaree, A.A.; Ahmed, S.A.; Salama, R.S. Enhanced catalytic activity for CO oxidation by highly active Pd nanoparticles supported on reduced graphene oxide/copper metal organic framework. *J. Taiwan Inst. Chem. Eng.* **2021**, *128*, 194–208. [CrossRef]
41. Norouzi, A.; Nezamzadeh-Ejhieh, A. Investigation of the simultaneous interactions of experimental variables and mechanism pathway in the photodegradation of methylene blue by binary ZnO/Cu_2O photocatalyst. *Mater. Res. Bull.* **2023**, *164*, 112237. [CrossRef]
42. Madkhali, N.; Prasad, C.; Malkappa, K.; Choi, H.Y.; Govinda, V.; Bahadur, I.; Abumousa, R.A. Recent update on photocatalytic degradation of pollutants in waste water using TiO_2-based heterostructured materials. *Results Eng.* **2023**, *17*, 100920. [CrossRef]
43. Benz, D.; Bui, H.V.; Hintzen, H.T.; Kreutzer, M.T.; Ommen, J.R.V. Mechanistic insight into the improved photocatalytic degradation of dyes for an ultrathin coating of SiO_2 on TiO_2 (P25) nanoparticles. *Chem. Eng. J. Adv.* **2022**, *10*, 100288. [CrossRef]
44. Jandaghian, F.; Pirbazari, A.E.; Tavakoli, O.; Asasian-Kolur, N.; Sharifian, S. Comparison of the performance of Ag-deposited ZnO and TiO_2 nanoparticles in levofloxacin degradation under UV/visible radiation. *J. Hazard. Mater. Adv.* **2023**, *9*, 100240. [CrossRef]
45. Banoth, P.; Kandula, C.; Lavudya, P.K.; Akaram, S.; Valladares, L.D.L.S.; Ammanabrolu, R.; Mamidipudi, G.K.; Kollu, P. $BiFeO_3$-Black TiO_2 Composite as a Visible Light Active Photocatalyst for the Degradation of Methylene Blue. *ACS Omega* **2023**, *8*, 18653–18662. [CrossRef] [PubMed]
46. Gebremariam, G.K.; Jovanović, A.Z.; Pašti, I.A. The effect of electrolytes on the kinetics of the hydrogen evolution reaction. *Hydrogen* **2023**, *4*, 776–806. [CrossRef]
47. Huang, Y.; Wang, C.; Wang, R.; Zhang, Y.; Li, D.; Zhu, H.; Wang, G.; Zhang, X. Ethanol solution plasma loads carbon dots onto 2D HNb_3O_8 for enhanced photocatalysis. *ACS Appl. Mater. Interfaces* **2023**, *15*, 1157–1166. [CrossRef] [PubMed]

48. Huang, K.; Li, C.; Zheng, Y.; Wang, L.; Wang, W.; Meng, X. Recent advances on silver-based photocatalysis: Photocorrosion inhibition, visible-light responsivity enhancement, and charges separation acceleration. *Sep. Purif. Technol.* **2022**, *283*, 120194. [CrossRef]
49. Weng, B.; Qi, M.Y.; Han, C.; Tang, Z.R.; Xu, Y.J. Photocorrosion inhibition of semiconductor-based photocatalysts: Basic principle, current development, and future perspective. *ACS Catal.* **2019**, *9*, 4642–4687. [CrossRef]
50. Zhu, J.; Cao, X.; Li, J. Ethanol-Induced Aggregation of Nonpolar Nanoparticles in Water/Ethanol Mixed Solvents. *Langmuir* **2022**, *38*, 13910–13915. [CrossRef]
51. Pentsak, E.O.; Cherepanova, V.A.; Sinayskiy, M.A.; Samokhin, A.V.; Ananikov, V.P. Systematic study of the behavior of different metal and metal-containing particles under the microwave irradiation and transformation of nanoscale and microscale morphology. *Nanomaterials* **2019**, *9*, 19. [CrossRef]
52. Periyat, P.; Leyland, N.; McCormack, D.E.; Colreavy, J.; Corr, D.; Pillai, S.C. Rapid microwave synthesis of mesoporous TiO_2 for electrochromic displays. *J. Mater. Chem.* **2010**, *20*, 3650–3655. [CrossRef]
53. Tauc, J.; Grigorovici, R.; Vancu, A. Optical properties and electronic structure of amorphous germanium. *Phys. Status Solidi B* **1966**, *15*, 627–637. [CrossRef]